



Predicting radar attenuation within the Antarctic ice sheet

Kenichi Matsuoka^{a,*}, Joseph A. MacGregor^{b,1}, Frank Pattyn^{c,2}

^a Norwegian Polar Institute, Fram Center, Tromsø 9296, Norway

^b Institute for Geophysics, The University of Texas at Austin, 10100 Burnet Rd., Bldg 196 (R2200), Austin, TX 78758, USA

^c Laboratoire de Glaciologie, Université Libre de Bruxelles, Avenue F.D. Roosevelt, B-1050 Bruxelles, Belgium

ARTICLE INFO

Article history:

Received 4 September 2012

Received in revised form

16 October 2012

Accepted 17 October 2012

Editor: P. Shearer

Available online 10 November 2012

Keywords:

Antarctic ice sheet
radar remote sensing
englacial attenuation
subglacial environment
thermo-mechanical modeling

ABSTRACT

To better understand the ability of ice-penetrating radar to diagnose the subglacial environment from bed-returned power, we model the englacial radar attenuation of Antarctic ice. First, we use a one-dimensional thermo-mechanical model to evaluate the sensitivity of the depth-averaged attenuation rates to ice temperature as a function of surface accumulation rate, geothermal flux, and ice thickness. We find that attenuation is most sensitive to variations in geothermal flux and accumulation rate when the bed temperature is close to the pressure-melting point. But even if geothermal flux and accumulation rate remain fixed, attenuation can easily vary with ice thickness. Such high sensitivities show that one should not assume a uniform attenuation rate in the radar data analysis. Then, using ensembles of modeled ice temperatures with different boundary conditions, we generate multiple attenuation predictions for the Antarctic ice sheet and evaluate the resulting uncertainties. The largest contributor to uncertainty in these predictions is the geothermal flux. This uncertainty is localized within the deeper half of the ice sheet. By combining these temperature ensembles with ice-core chemistry data, we show that the sea salt adds little to the attenuation, but the contribution from acids accounts for ~29% (inland) to ~53% (coast) of the total attenuation. We conclude that improving radar diagnosis of the subglacial environment using bed-returned power requires both (1) better data-interpretation algorithms that account for attenuation variations and (2) better constraints of geothermal flux and bulk chemistry.

© 2012 Elsevier B.V. All rights reserved.

1. Introduction

Satellite observations of anomalous changes in ice-sheet surface elevation led to a paradigm shift in our understanding of the Antarctic subglacial environment (Gray et al., 2005; Wingham et al., 2006; Fricker et al., 2007). Subglacial hydraulic networks are now understood to transfer water on the timescales of months to years, and active subglacial lakes have variable linkages between them (Smith et al., 2009). Most such lakes lie upstream of the fast-flowing glaciers that discharge much of the Antarctic ice into the oceans (Stearns et al., 2008; Rignot et al., 2011). Field observations of spatiotemporal variations of the subsurface of the ice sheets are thus crucial for understanding the dynamics and future sea-level contributions of the Antarctic ice sheet.

Ground-based and airborne ice-penetrating radar has been used widely to characterize the basal interface. Spatial variations of bed-returned power have been accepted as an indication of a

distinct variation of the bed conditions; higher returned power is taken to indicate either a subglacial lake (e.g., Siegert et al., 2005; Carter et al., 2007, 2009) or a thawed bed (Bentley et al., 1998; Fujita et al., 2012; Rippin et al., 2004; Jacobel et al., 2009, 2010). However, the bed-returned power is attenuated by the ice overburden that the radio waves travel through, and recent studies have demonstrated that the attenuation rates in ice sheets are rarely uniform (Matsuoka, 2011; MacGregor et al., 2012). These studies explored attenuation rates for only a narrow range of glaciological conditions, so our understanding of radar attenuation across Antarctica remains incomplete. Thus, assessing the spatial variability of englacial radar attenuation is a central problem facing the use of radar for determining the nature of the subglacial environment.

Here, we first analyze the sensitivity of attenuation upon the ice-sheet boundary conditions and then make predictions of attenuation throughout the entire present-day Antarctic ice sheet. We examine the sensitivity of attenuation by first calculating just the pure-ice contribution using depth profiles of ice temperature from a one-dimensional model. We then predict the continent-wide spatial variation of the pure-ice contribution to the englacial attenuation using temperature outputs from a suite of thermo-mechanical model ensemble runs of the ice sheet. Finally,

* Corresponding author. Tel.: +47 77 75 06 45.

E-mail addresses: matsuoka@npolar.no (K. Matsuoka), joemac@ig.utexas.edu (J.A. MacGregor), fpattyn@ulb.ac.be (F. Pattyn).

¹ Tel.: +1 512 471 0411.

² Tel.: +32 2 650 28 46.

we explore how the ice chemical composition affects ice-sheet-wide variations of the attenuation.

2. Background and methods

2.1. Effects of englacial attenuation on bed-returned power

The returned power from the bed P depends on bed reflectivity R as well as ice properties integrated along the two-way travel path to the bed. The three major travel-path effects on the radio-wave propagation are geometric spreading G , dielectric attenuation L , and signal reduction B due to birefringence (Matsuoka et al., 2010). In the decibel scale ($[x]_{\text{dB}} = 10 \log_{10} x$), the bed-returned power is

$$[P]_{\text{dB}} = [S]_{\text{dB}} - [G]_{\text{dB}} + [R]_{\text{dB}} - [L]_{\text{dB}} - [B]_{\text{dB}}, \quad (1)$$

where S represents instrumental factors.

The term G is a function of radar height h above the surface, ice thickness H , and the depth-averaged relative permittivity ε (~ 3.2): $[G]_{\text{dB}} = 2[h + H/\sqrt{\varepsilon}]_{\text{dB}}$. When H greatly exceeds the firn-layer thickness (~ 100 m), density variations which alter the permittivity affect G by less than 0.05 dB (Matsuoka et al., 2010). Therefore, it is common to calculate the geometrically corrected returned power P^c from the measured returned power by subtracting the geometric spreading for a uniform permittivity:

$$[P^c]_{\text{dB}} = [P]_{\text{dB}} + [G]_{\text{dB}} = [S]_{\text{dB}} + [R]_{\text{dB}} - [L]_{\text{dB}} - [B]_{\text{dB}}. \quad (2)$$

Birefringent effects B vary as a function of the magnitude of anisotropy in the ice-crystal alignments (ice fabrics), and the principal axes of ice fabrics. Over the full range of these variables, the probability that B varies more than 5 dB and 10 dB is 12% and 3%, respectively (Fujita et al., 2006). Moreover, the principal axes of the crystal alignments have known relations to surface strain rates in central West Antarctica (Matsuoka et al., 2012a), so proper survey design can mitigate the confounding effect of birefringence. Therefore, P^c is mostly a function of bed reflectivity and englacial attenuation.

When the bed is smooth and flat relative to the wavelength of the radio wave in ice (~ 1 –100 m), the bed reflectivity can be approximated by the Fresnel reflectivity. Contrasts in Fresnel reflectivity between thawed and frozen ice-sheet beds are ~ 10 –15 dB (Peters et al., 2005). This range is thus an upper limit to the uncertainty in the englacial two-way attenuation L , with which P^c can become a proxy for the bed reflectivity R . To constrain R within 10 dB, the one-way depth-averaged attenuation rate $\langle N \rangle (= [L]_{\text{dB}}/(2H))$ should be known to better than 2.5 or 1.7 dB/km when the ice is 2- or 3-km thick, respectively. Otherwise, variations in the bed-returned power begin to be dominated by uncertainty in attenuation.

2.2. Attenuation parameterization

The depth-averaged attenuation rate $\langle N \rangle$ is determined from the depth profile of the one-way local attenuation rate $N(z)$:

$$\langle N \rangle_0^H = \frac{[L]_{\text{dB}}}{2H} = \frac{1}{2H} \int_0^H N(z) dz. \quad (3)$$

The one-way local attenuation rate N (dB/km) is proportional to local ice conductivity σ (Winebrenner et al., 2003)

$$N(z) = \frac{1000(10 \log_{10} e)}{c \varepsilon_0 \sqrt{\varepsilon}} \sigma(z) \approx 0.914 \sigma(z), \quad (4)$$

where ε_0 is the permittivity of free space.

Ice conductivity in polar ice sheets depends on contributions from pure ice (subscript $i=0$) and two chemical constituents: acidity ($i=1$) and sea salt ($i=2$). Each component has an Arrhenius-type dependence on ice temperature T (Moore and Fujita, 1993; MacGregor et al., 2007):

$$\sigma = \sum_{i=0}^2 \sigma_i^0 C_i \exp \left[-\frac{E_i}{k} \left(\frac{1}{T} - \frac{1}{T_r} \right) \right], \quad (5)$$

where σ_i^0 is the pure-ice conductivity ($i=0$) or molar conductivities ($i=1, 2$) at the reference temperature $T_r=251$ K. Acid and sea salt contributions depend linearly on their radar-effective concentrations C_1 and C_2 , which depend on in-situ conditions of soluble ions at the ice temperature (see MacGregor et al. (2007) for details). Here C_0 is defined as unity, E_i are activation energies corresponding to individual components, and k is the Boltzmann constant. σ_i^0 and E_i are frequency independent over the HF and VHF ranges (Fujita et al., 2000). For this study, we used $\sigma_0^0=9.2 \mu\text{S/m}$, $\sigma_1^0=3.2 \text{ S/m/M}$ (where $\text{M}=\text{mol/L}$), $\sigma_2^0=0.43 \text{ S/m/M}$, $E_0=0.51 \text{ eV}$, $E_1=0.20 \text{ eV}$, and $E_2=0.19 \text{ eV}$ (MacGregor et al., 2012). Fig. 1a shows the temperature dependencies of the pure-ice and acid contributions to the local attenuation rate N calculated using Eqs. (4) and (5).

2.3. Ice-temperature modeling

Estimating depth-averaged attenuation rates $\langle N \rangle$ using Eqs. (3)–(5) requires estimates of depth profiles of ice temperature. For different purposes, we modeled ice temperature in two ways.

First, to examine the sensitivity of depth-averaged attenuation rates on ice-sheet boundary conditions, a steady-state one-dimensional heat flow model is coupled with a kinematic ice-flow model (Matsuoka, 2011; Morse et al., 2002). The kinematic model approximates the depth profiles of horizontal ice velocity with two piecewise linear functions. The thickness of the bottom

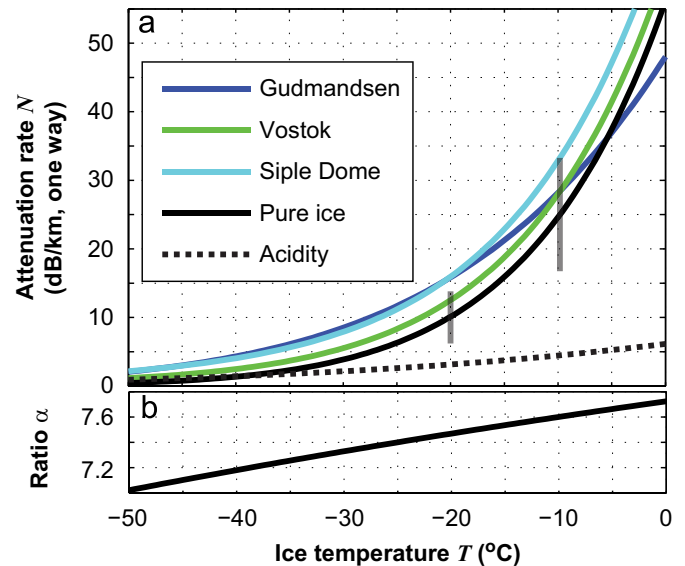


Fig. 1. (a) Temperature dependence of the attenuation contributions from pure ice ($i=0$ in Eq. (5)) and acid ($i=1$), when radar-effective acidity (C_1) is $1 \mu\text{M}$. Also shown are a parameterization using a single Arrhenius form for the conductivity of meteoric ice that implicitly includes chemistry contributions (Gudmandsen, 1971), ice with soluble ions at levels of depth-averaged acidity and salinity at Siple Dome in West Antarctica ($C_1=1.2 \mu\text{M}$; C_2 , from sea salt, $=4.1 \mu\text{M}$) (MacGregor et al., 2007), and similarly for Vostok in East Antarctica ($C_1=0.5 \mu\text{M}$; $C_2=2.0 \mu\text{M}$) (MacGregor et al., 2009). In Gudmandsen's (1971) parameterization, pre-exponential coefficient is $15.4 \mu\text{S/m}$ and the activation energy is 0.33 eV . The two gray vertical bars are uncertainties of the pure-ice contribution estimated with standard deviations in dielectric measurements (MacGregor et al., 2007). (b) Ratio α (%) of the attenuation contribution from acid to that from sea salt (Eq. (6)) as a function of ice temperature.

softer layer in the model is assumed to be $0.2H$, a value that gives a good approximation at flank sites at least one ice thickness away from an ice-flow divide (Neumann et al., 2008). This approximation is valid for most of inland Antarctica. Horizontal advection is not included, and all boundary conditions are kept steady in each experiment. To assess the spatial variations of attenuation rates across the Antarctic ice sheet, we use the temperature fields from Pattyn (2010), which had been calculated using a three-dimensional, hybrid, steady-state, thermo-mechanically coupled ice sheet model. The ice temperature field is calculated at 5-km horizontal resolution with 21 layers in the vertical. Within the ice shelves, ice temperature is determined analytically by accounting only for vertical heat conduction and advection, and by balancing the basal and surface mass-balance rates. For the remainder of the ice sheet, ice temperature is calculated numerically by accounting for heat advection, vertical heat diffusion and internal strain heating. Ice-velocity fields are set to maintain the balance fluxes, and depth profiles of the velocity fields are consistent with the dominant horizontal stress gradients over subglacial lakes and ice streams. The horizontal stress gradients are taken into account only in fast-flowing areas (> 100 m/a). Basal sliding over grounded ice is calculated when the bed is thawed. See Pattyn (2010) for more details.

2.4. Boundary conditions for continent-wide temperature fields

Englacial temperatures vary as a function of ice thickness H , surface accumulation rate AR , surface temperature T_s , and geothermal flux GF . Example estimates of these parameters for the current

Antarctic ice sheet are shown in Fig. 2. Except for the Antarctic Peninsula and the coastal area, H generally exceeds 2 km. We examine attenuation mainly for such inland ice because spatial variations in attenuation rates are more likely to hamper diagnosis of bed conditions there (Eq. (3)).

For investigations using the one-dimensional model, we varied the ice thickness H from 2 to 4 km, the surface accumulation rate AR from 0.02 to 0.5 m/a, and the geothermal flux GF from 30 to 120 mW/m². The portion of Antarctica where the ice thickness exceeds 2 km is roughly the same as that where the surface temperature T_s is below -30 °C, so we assumed surface temperatures of -30 and -40 °C.

The thermo-mechanically coupled ice sheet model was run for 24 sets of boundary conditions, keeping ice thickness and surface temperature at the current values (Fig. 2a). The predicted bed conditions for these model runs are presented by Pattyn (2010). Surface accumulation rate is obtained from Van de Berg et al. (2006), based on the output of a regional atmospheric model for the past 25 yr (accumulation rate dataset ARO). For this study, we also used two additional accumulation-rate datasets (AR1 and AR2) to account for decadal anomalies in regional patterns of accumulation (Monaghan et al., 2006); these datasets constitute the uncertainty in ARO. Because little is known about geothermal flux in Antarctica, we ran ensemble models with eight geothermal flux fields. The six geothermal flux fields are based on Fox-Maule et al. (2005) (FM), Shapiro and Ritzwoller (2004) (SR), and Pollard et al. (2005) (P): FM, SR, P, (FM+SR)/2, (SR+P)/2, and (FM+SR+P)/3. Because FM and P have similar spatial patterns, we do not consider (FM+P)/2. In addition, we used two uniform values (42 and 54 mW/m²,

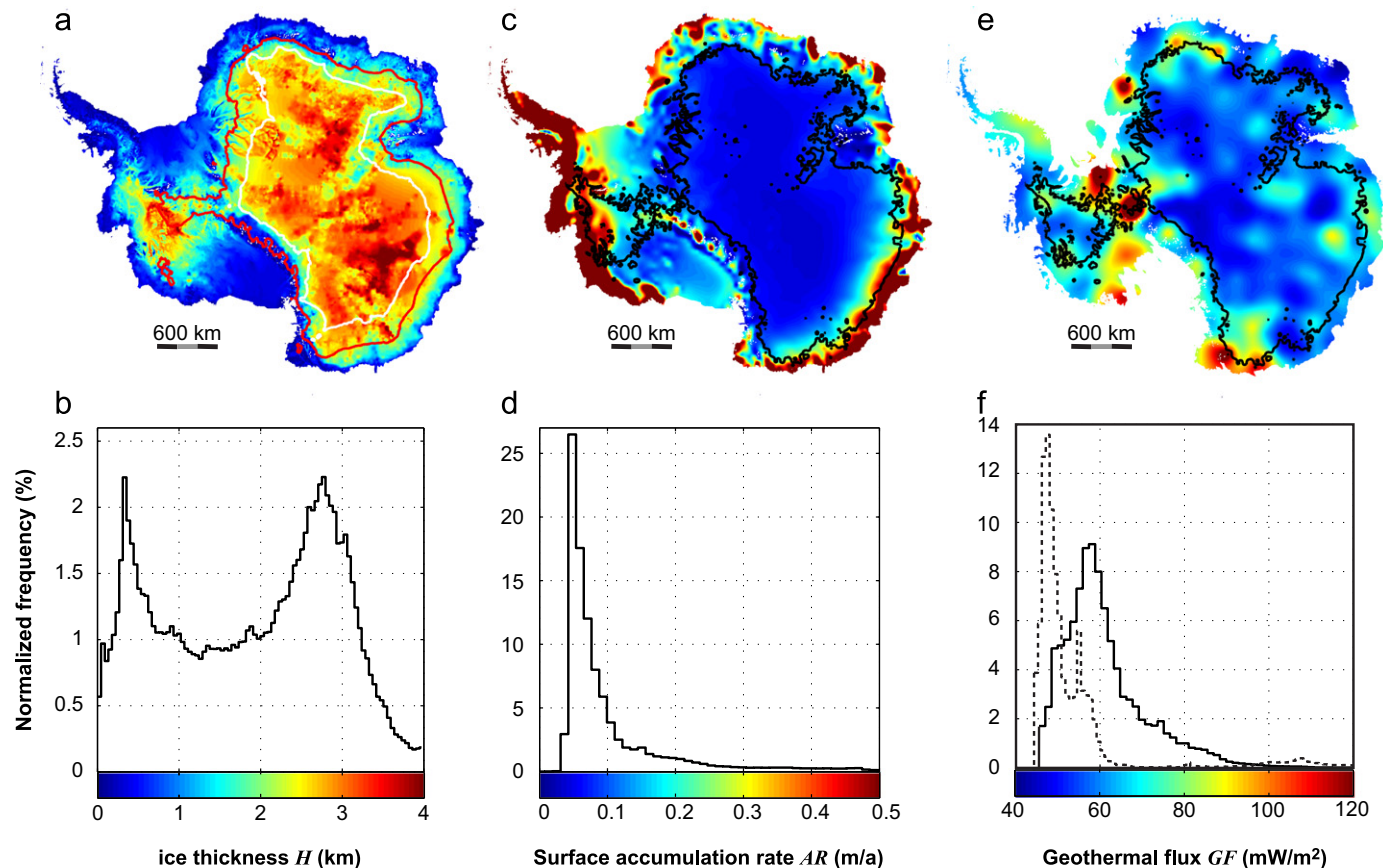


Fig. 2. Maps of (a) ice thickness, (c) surface accumulation rate (Van de Berg et al., 2006), and (e) geothermal flux (Fox-Maule, et al., 2005) in the present-day Antarctic ice sheet as compiled by Le Brocq et al. (2010). The geothermal flux excludes areas over ice shelves. The lower row shows normalized (%) histograms for (a), (c), and (e) together with the color legends. For (d) and (f), the histogram data are for areas where ice is thicker than 2 km only, which is bound by black contours in panels (c) and (e). The dashed curve in panel (f) shows the histogram for another geothermal flux dataset (Shapiro and Ritzwoller, 2004). In (a), contours show the surface temperatures of -30 °C (red) and -40 °C (white) (Comiso, 2000).

the numerical values of which are frequently used as references in continent-scale Antarctic and Greenland ice-sheet modeling studies (e.g., Payne et al., 2000; Huybrechts, 2002; Pattyn, 2003).

Boundary conditions are tuned so that the model predicts a thawed bed over known subglacial lakes and ice streams and also replicates depth profiles of the ice temperature measured at deep boreholes (Pattyn, 2010). For this tuning, Pattyn (2010) treated all ice streams and three lake types as thawed: definite lakes, which return a radar power at least 2 dB larger than their surroundings (Carter et al., 2007); fuzzy lakes, defined by high absolute and relative bed reflectivity but are not specular (Carter et al., 2007); and active lakes, which cause ice-surface vertical motions detected by the satellite altimetry (Smith et al., 2009). The model is run for steady-state conditions, but the real ice-temperature field may be transient. Adjusting the boundary conditions to replicate the ice temperature measured at deep boreholes also accounts for some of the effects of long-term evolution of the ice sheet. The ensemble mean of these 24 experiments shows that the base of 55% of the Antarctic ice sheet (excluding ice shelves) is at the pressure-melting point (Pattyn, 2010).

3. Results

Depth profiles of temperature and its ice-sheet-wide spatial variation are put into Eq. (5) so we can use Eqs. (3) and (4) to estimate local attenuation rates and depth-averaged attenuation rates. We first consider the pure-ice contribution only (i.e., we explicitly neglect the chemistry contributions), and later assess chemical effects. This approach is undertaken because the pure-ice contribution dominates the attenuation rates (Fig. 1a) and relatively little is known about englacial chemistry across the entire Antarctic ice sheet. Also, contributions from pure ice and

chemicals do not interfere with each other; rather, the total attenuation is the sum of their contributions (Eq. (5)).

3.1. Sensitivity to boundary conditions

By evaluating modeled depth-averaged attenuation rates $\langle N \rangle$ in terms of surface accumulation rates and geothermal flux (Fig. 3), we find three distinct features regardless of the ice thickness and surface temperature.

The first feature occurs when the surface accumulation rate is large and the geothermal flux is small, both of which tend to cool the ice column. In these cases, $\langle N \rangle$ is relatively insensitive to both parameters. The second behavior occurs when the bed is thawed (i.e., the basal temperature T_{bed} is at the pressure melting point PMP). Here, $\langle N \rangle$ is independent of the geothermal flux and insensitive to the surface accumulation rate. This is because the vertical heat conduction becomes independent of the magnitude of geothermal flux, though a larger geothermal flux results in additional basal melting. Basal melting rates are typically of the order of $\sim 10^{-3}$ m/a, which is generally much smaller than the surface accumulation rate, so that vertical advection due to basal melting is insignificant. Finally, the third feature occurs when the bed is barely frozen (i.e., T_{bed} is close to the PMP). In such cases, $\langle N \rangle$ is sensitive to variations both in geothermal flux and surface accumulation rate. Lower surface temperatures make $\langle N \rangle$ more sensitive to geothermal flux changes, whereas higher surface temperatures render $\langle N \rangle$ more sensitive to the surface accumulation rate. This behavior occurs because the attenuation rates depend exponentially on ice temperature, and the surface temperature affects the ice temperature at greater depths when the surface accumulation rate is larger.

The attenuation rate is relatively insensitive to surface accumulation rate AR in two regimes (Fig. 4): when AR is small enough

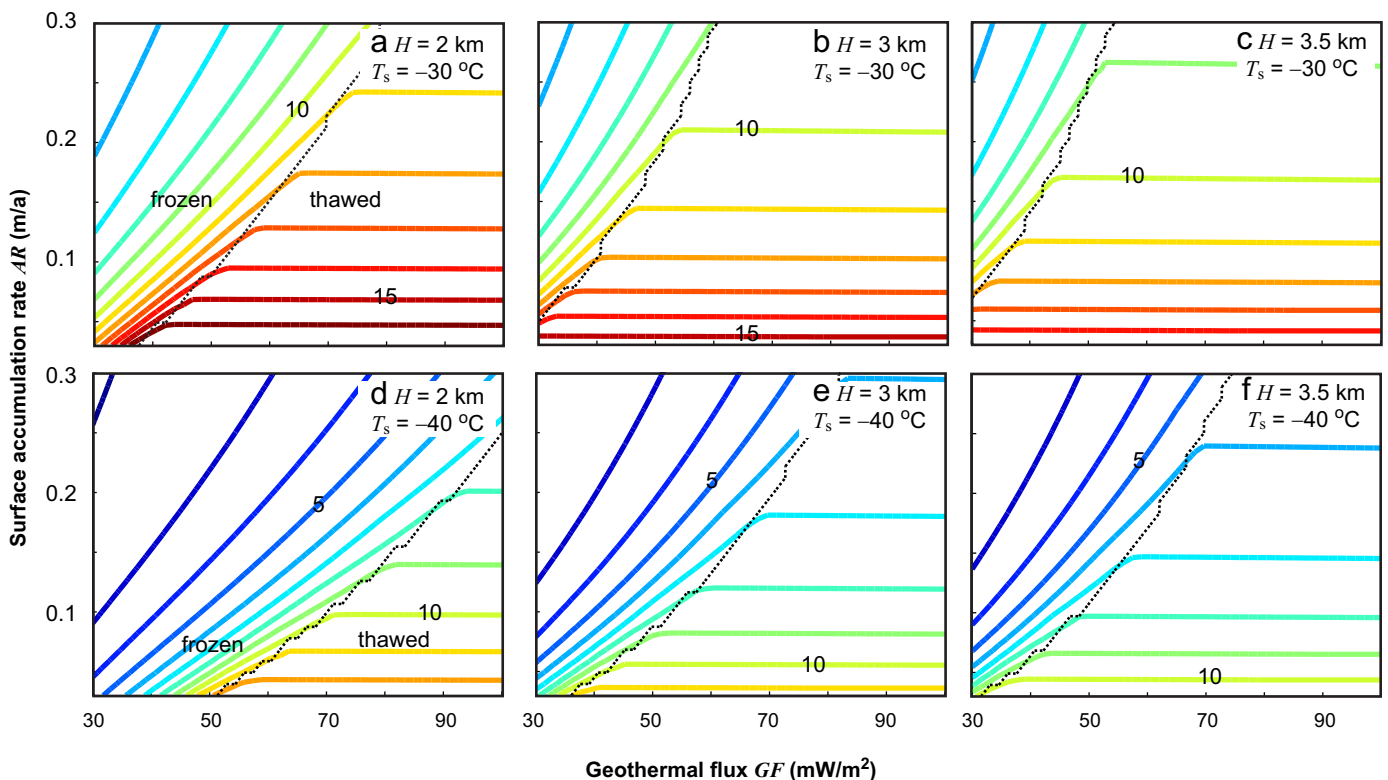


Fig. 3. One-way depth-averaged attenuation rates $\langle N \rangle$ in terms of surface accumulation rate and geothermal flux. Colored curves mark contour values ranging from 2 to 16 dB/km in steps of 1 dB/km. Each panel represents a different combination of ice thickness H and surface temperature T_s . Dashed curves show the boundary between frozen and thawed beds.

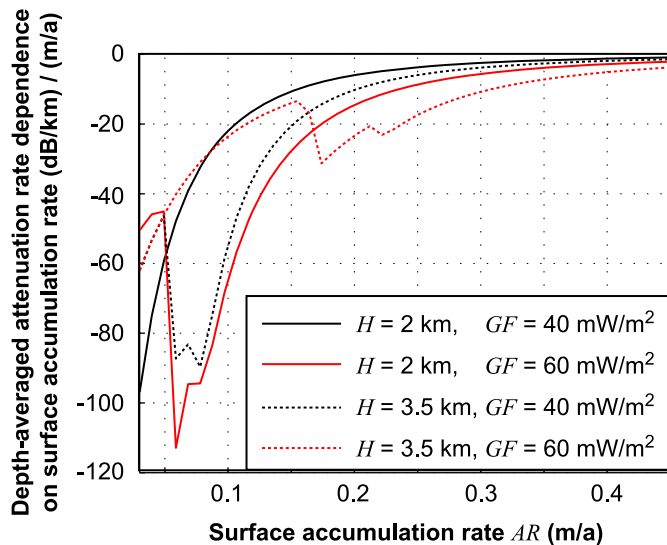


Fig. 4. Sensitivity $d\langle N \rangle/dAR$ of the depth-averaged attenuation rate to surface accumulation rate for several values of ice thickness H and geothermal flux GF . The surface temperature is fixed at -40°C .

that the bed is thawed (e.g., $AR < 0.05$ m/a when $H=2$ km, $GF=60$ mW/m²), and when AR is large enough to keep the bed well below the PMP (e.g., $AR > 0.1$ m/a when $H=2$ km, $GF=60$ mW/m²). Between these two regimes, $\langle N \rangle$ is at least ~ 1.5 times more sensitive to the surface accumulation rate. As an extreme example when $H=2$ km and $GF=60$ mW/m², $\langle N \rangle$ varies approximately 1 dB/km per 1 cm/a variation in the surface accumulation rate. This variation corresponds to variations of ~ 8 dB in the two-way attenuation L for 2-km-thick ice, when the surface accumulation rate varies between 6 and 8 cm/a.

Fig. 5 shows the geothermal flux dependence $d\langle N \rangle/dGF$. $\langle N \rangle$ varies ~ 2 dB/km for a geothermal flux variation of 10 mW/m². And $\langle N \rangle$ varies more when the surface temperature is higher and the ice is thicker.

3.2. Ice thickness dependence

Radar-data analyses commonly assume that attenuation rates are independent of the ice thickness. With this assumption, the depth dependence of the bed returned power can be interpreted as a proxy of the depth-averaged attenuation rate if bed reflectivity is ice thickness independent (i.e., $d[P^c]_{dB}/dH \sim d[L]_{dB}/dH = 2\langle N \rangle$; Eqs. (2) and (3)). Though the assumption is convenient, is it accurate? Our modeling indicates otherwise: even when all boundary conditions remain unchanged but only ice thickness varies, the depth-averaged attenuation rates do not remain the same (Fig. 6a).

Where ice thickness is small enough to keep the bed frozen for a given combination of the boundary conditions (profile A), $\langle N \rangle$ increases slightly as the ice thickens. In contrast, when the ice is thick enough to keep the bed thawed, shown as profile E, $\langle N \rangle$ decreases as the ice thickens. Moreover, profile E has a steeper slope. The other three profiles B, C, and D show cases when the bed conditions change as the ice thickness varies; as the ice becomes thicker, $\langle N \rangle$ increases when the bed is frozen but decreases when thawed.

These predicted variations in $\langle N \rangle$ can potentially compromise radar-data analyses assuming that $\langle N \rangle$ is regionally uniform. The degree of this compromise can be measured according to the range of $\langle N \rangle$ for a given ice thickness range (Fig. 6b and c). The range of $\langle N \rangle$ is small (< 1 dB/km) when the bed is always frozen. However, $\langle N \rangle$ varies more rapidly when the bed is barely frozen

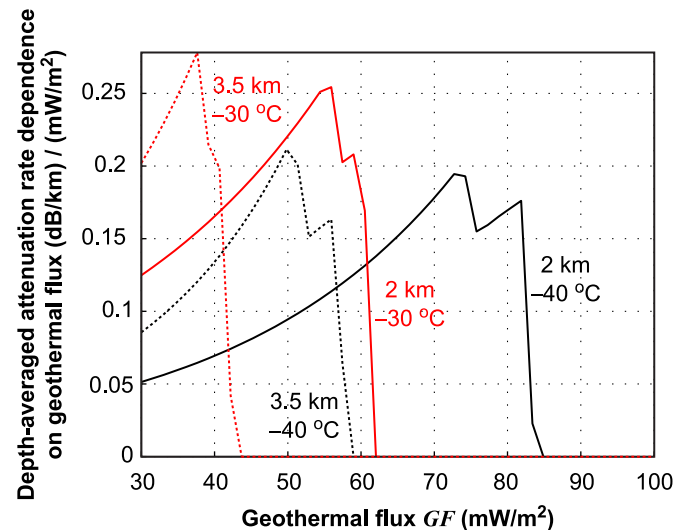


Fig. 5. Sensitivity $d\langle N \rangle/dGF$ of the depth-averaged attenuation rate to the geothermal flux for several values of ice thickness and surface temperature. The surface accumulation rate is fixed at 0.3 m/a.

or when the bed becomes thawed as the ice thickness approaches the upper limit of the given thickness range (e.g., profile C for $2.5 < H < 3.5$ km). When these conditions apply with smaller geothermal flux and lower surface accumulation rate, $\langle N \rangle$ can vary up to 3 dB/km due to ice-thickness changes alone. In central East Antarctica, ice thickness varies 2–3 km in midstream regions and 2.5–3.5 km in upstream regions (Fig. 2a); the range of the modeled ice thickness dependence of $\langle N \rangle$ (Fig. 6b and c) can be expected in these regions so accurate bed diagnosis can be hampered.

3.3. Continent-wide distribution

3.3.1. Ensemble-mean field

Using the mean ice temperature from the 24 model experiments, we estimated the spatial distribution of the pure-ice contribution to $\langle N \rangle$. (The mean basal temperature corresponding to this ice-temperature field is shown in figure 3a of Pattyn (2010)). Fig. 7 shows that $\langle N \rangle$ is more than ~ 30 dB/km in the Siple Coast and Antarctic Peninsula regions, as well as in several coastal regions in East Antarctica. Most of the coastal margin also has a similarly high attenuation rate (~ 25 dB/km), although the Ross and Ronne–Filchner ice shelves have smaller $\langle N \rangle$ values (15–20 dB/km) than most of the smaller ice shelves. The majority of the West Antarctic Ice Sheet has intermediate $\langle N \rangle$ values (10–15 dB/km). Variations in $\langle N \rangle$ over inland East Antarctica are noticeably smaller than the other regions (< 10 –15 dB/km). However, $\langle N \rangle$ can still vary more than 2–3 dB/km over a horizontal distance of 50–100 km. Such local variability agrees with more detailed attenuation modeling along the Vostok flowline (MacGregor et al., 2012). Since ice is thicker than 3 km in most of East Antarctic inland (Fig. 2a), these relatively small variations in $\langle N \rangle$ can easily result in more than 10-dB differences in predicted L over horizontal distances of 50–100 km. In the inland regions, ice flows more uniformly than that in the coastal regions, which may give the false impression that the attenuation rates vary little. However, the inland combination of a modest uncertainty in $\langle N \rangle$ with thick ice makes predictions of L challenging.

The subglacial environment affects the range of attenuation rates. For instance, $\langle N \rangle$ ranges by 15.1 ± 6.2 dB/km (mean \pm standard deviation) for ice shelves and 16.7 ± 17.2 dB/km for

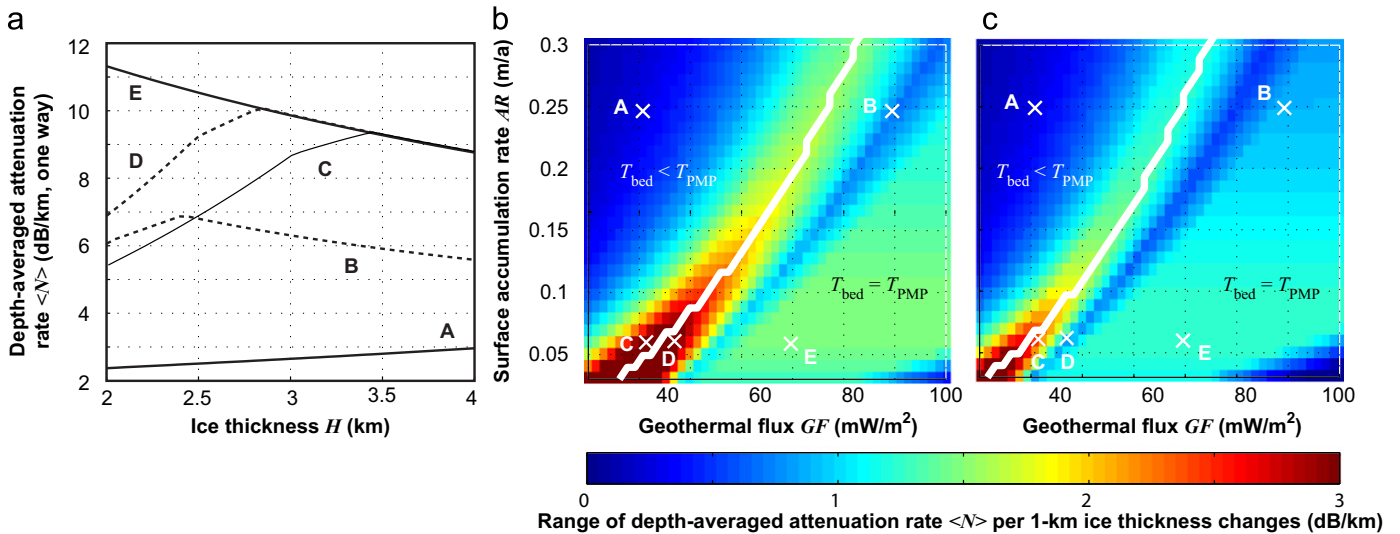


Fig. 6. Relationships between depth-averaged attenuation rate $\langle N \rangle$ and ice thickness. (a) $\langle N \rangle$ for five cases of geothermal flux GF and surface accumulation rate AR . (b) Values of GF and AR for the five cases and the range (maximum–minimum) of $\langle N \rangle$ for $H=2-3$ km. (c) Same as (b) but for the range of $2.5-3.5$ km. The cases are as follows: (A) bed is always frozen, (B, C, D) bed alternates from frozen to thawed as ice becomes thicker, and (E) bed is always thawed. The white curves in (b) and (c) show the boundary between the following two domains: the bed is always frozen regardless of the ice thickness (left top); the bed becomes thawed at a certain ice thickness or is always thawed (right bottom). Surface temperature is -40 °C for all cases.

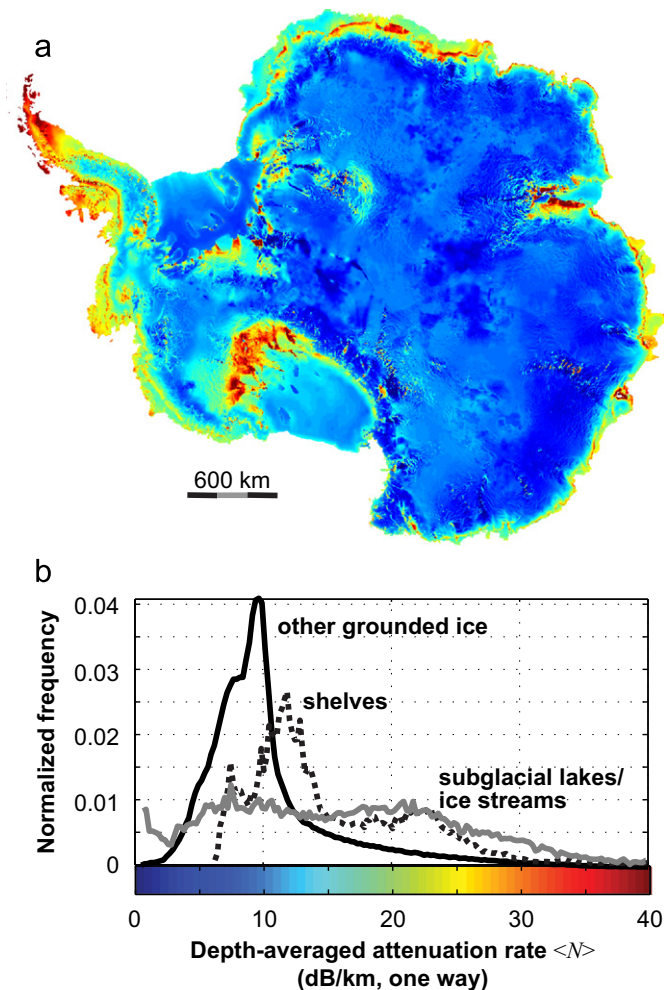


Fig. 7. Depth-averaged attenuation rates $\langle N \rangle$ derived from the ensemble-mean ice temperature field. (a) Map. (b) Histogram and color code for (a). The histogram is divided into areas overlying subglacial lakes and ice streams (6% of the entire model domain), other grounded ice (83%), and ice shelves (11%). Only the pure-ice contribution is considered.

Table 1

Mean and standard deviation of depth-averaged attenuation rates (dB/km, one way) over the Antarctic ice sheet and ice shelves.

Geothermal flux dataset	Surface accumulation rate dataset		
	ARO ^a	AR1	AR2
FM ^a	15.6 ± 6.1	15.6 ± 6.1	15.6 ± 6.1
SR	15.1 ± 6.4	15.1 ± 6.4	15.1 ± 6.4
FM+SR	15.4 ± 6.2	15.4 ± 6.2	15.4 ± 6.2
P	15.1 ± 6.2	15.1 ± 6.2	15.1 ± 6.2
P+SR	15.1 ± 6.3	15.1 ± 6.3	15.1 ± 6.3
FM+P+SR	15.3 ± 6.2	15.3 ± 6.1	15.3 ± 6.1
Uniform, 42 mW/m ²	14.0 ± 6.5	14.0 ± 6.4	14.0 ± 6.4
Uniform, 54 mW/m ²	15.1 ± 6.0	15.1 ± 6.0	15.1 ± 6.0

^a See Section 2.4 for definitions of these surface accumulation rate and geothermal flux dataset labels.

subglacial lakes and ice streams (Fig. 7b). In contrast, grounded ice that is neither fast-flowing nor over a subglacial lake has only 10.7 ± 7.3 dB/km, with a distinct median value of 9.2 dB/km. For grounded ice thicker than 2 km, attenuation rates are even lower at 8.5 ± 3.0 dB/km.

3.3.2. Prediction uncertainty

The continental-mean value of $\langle N \rangle$ is consistently $\sim 15-16$ dB/km for nearly all boundary conditions (Table 1). But when we applied a uniform geothermal flux of 42 mW/m², the value was only 14 dB/km. The standard deviation of $\langle N \rangle$ is roughly 6 dB/km for all datasets.

To examine effects of uncertainty from the surface accumulation rate, separate from that of geothermal flux, we calculated the depth-averaged attenuation in the upper half of the ice sheet. In shallow ice, variations in the surface accumulation rate dominate the temperature variations. Over the entire ice sheet and ice shelves, the range of the attenuation rates $\langle N \rangle_{0}^{0.52H}$ averaged from the ice-sheet surface to 52% of the local ice thickness is only 0.2–0.3 dB/km (Fig. 8a). Even where the ice is 4-km thick, the variation over $0.52H$ yields variations in L less than about 1 dB, which is much smaller than the other uncertainties. Therefore, these

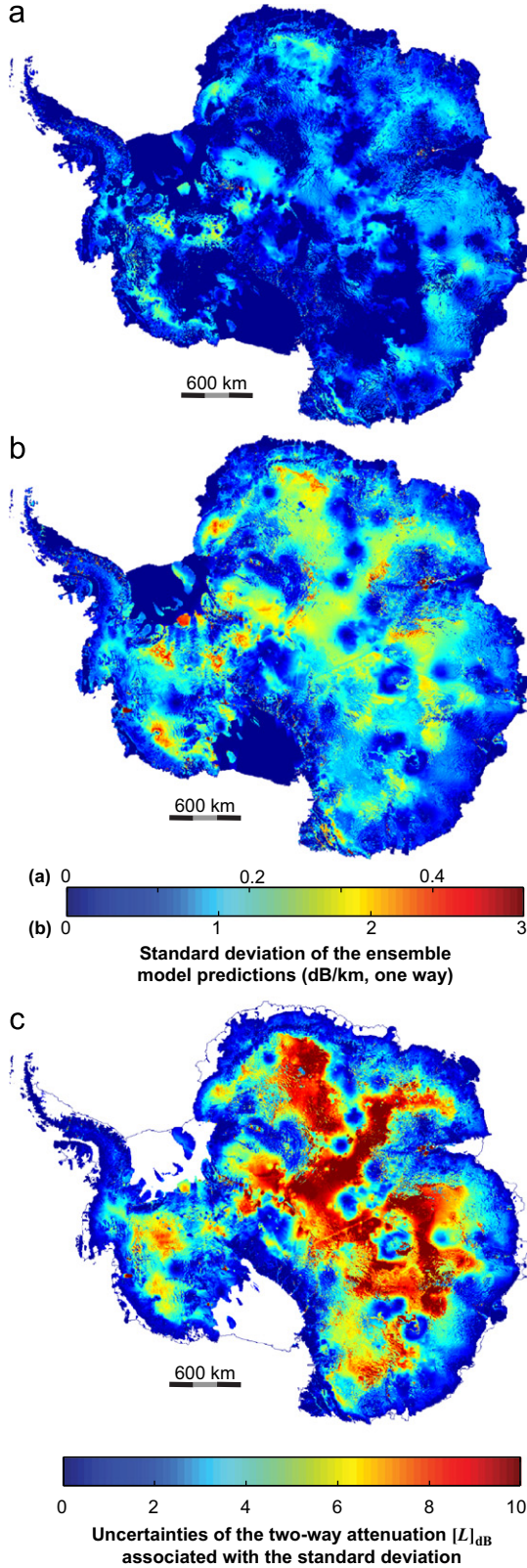


Fig. 8. Uncertainty of the predicted attenuation based on the model ensembles. (a) Standard deviation of depth-averaged attenuation rates for the upper 52% of the ice sheet $\langle N \rangle_0^{0.52H}$. (b) Same as (a) except for the entire ice column $\langle N \rangle_0^H$. (c) Uncertainty of the two-way attenuation L , estimated as the standard deviation (b) multiplied by the ice thickness (Fig. 2a). The color code is truncated at 10 dB. Small standard deviations over the ice shelves (panel b) are likely a modeling artifact (see text) so the uncertainty in L is not shown there.

variations indicate that uncertainty in the surface accumulation rate is not a critical concern for continent-wide attenuation predictions.

In contrast, the depth-averaged attenuation rate $\langle N \rangle_0^H$ for the entire ice column varies significantly with the assumed boundary conditions (Fig. 8b). For the majority of the ice sheet, variations of $\langle N \rangle_0^H$ over the 24 ensemble estimates exceed 1 dB/km, reaching ~ 2 dB/km in some areas. Because $\langle N \rangle$ varies little in the upper half of the ice sheet, most of this variability occurs in the lower half, where the geothermal flux uncertainty dominates the attenuation uncertainty. Thus, to accurately predict the attenuation, better constraints on the pattern of geothermal flux are needed.

The standard deviation of $\langle N \rangle$ ensembles over the ice shelves is small (Fig. 8b). The small variability arises because the ice temperature fields over the ice shelves were calculated by equating the basal and surface mass balance, so geothermal flux variations are irrelevant to floating ice (Pattyn, 2010). In reality, melting of the meteoric ice and accretion of marine ice at the lower boundary of the ice shelves alter the temperature field in the ice shelves. Therefore, the small variability we predict here is not indicative of the attenuation variability over the ice shelves. A more realistic modeling over the ice shelves requires estimating the basal mass balance by describing the ice–ocean interactions (e.g., Walker and Holland, 2007), which is beyond the scope of this paper. Thus, to predict the attenuation at a given location in ice shelves, we need to constrain the basal mass balance.

Areas near subglacial lakes, ice streams, and deep ice cores have anomalously small standard deviations in $\langle N \rangle_0^H$. The reason for the small values is rooted in the temperature modeling method. Pattyn (2010) increased the geothermal flux until the basal temperature reached the PMP over subglacial lakes and ice streams. The method also tuned the geothermal flux so that the predicted englacial temperature is close to the measured borehole-temperature profiles. This tuning affects areas up to 200 km away. Therefore, some of these tuned regions have a relatively small geothermal-flux uncertainty and thus show up as circular areas with low uncertainties in Fig. 8b. However, as most of these subglacial lakes and ice streams were originally identified using radar data, the temperature model's tuning to the PMP over the lakes and ice streams may introduce an error, if the attenuation correction was not appropriate.

We also examined the uncertainty in the two-way attenuation L (Fig. 8c). $[L]_{dB}$ has uncertainty equal to $2H$ times the standard deviation of $\langle N \rangle$ in the ensemble experiments. Uncertainties are less than several decibels in ice thinner than ~ 2 km (cf. Fig. 2a), including near the coast. Farther inland, the attenuation uncertainty exceeds ~ 10 dB in many areas in East Antarctica and 5–8 dB in West Antarctica. Isolated areas with anomalously low uncertainties are usually regions with low standard deviation of $\langle N \rangle$ rather than thinner ice.

3.4. Effects of ice chemistry

3.4.1. Relative importance of acidity and sea-salt contributions

We next consider the acid and sea-salt contributions to the attenuation. Activation energies for these contributions are roughly 40% of that of the pure-ice contribution, so their relative contributions are larger at lower temperatures (Fig. 1a); the ratio N_{acid}/N_{pure} of these contributions to the attenuation rate is 1.04 at -40 °C and 0.18 at -10 °C.

The importance α of the acid contribution relative to the sea-salt contribution can be described as $\alpha = \sigma_1/\sigma_2$ (Eq. 5), which equals

$$\alpha = \frac{\sigma_1^0}{\sigma_2^0} \exp \left[-\frac{E_1 - E_2}{k} \left(\frac{1}{T} - \frac{1}{T_r} \right) \right] \quad (6)$$

The molar conductivity for acidity σ_0^a is ~ 7.4 times larger than that for sea salt and activation energies for these two components are similar. So, α is roughly 7.4 over the full temperature range in the ice sheet (Fig. 1b). Therefore, for equivalent concentrations, the sea-salt contribution to the local attenuation rate N is only $\sim 14\%$ of the acid contribution.

3.4.2. Continent-wide distribution of acidity and sea salt

To explore the effect of a spatially varying chemical composition on the attenuation rates, we examined the relationship between ice-core chemistry data and site conditions. We first derived radar-effective acidity and sea-salt concentrations using soluble-chemistry and ice-temperature data from the ice cores drilled at Siple Dome (MacGregor et al., 2007), South Pole (Cole Dai, 2004), Taylor Dome (Mayewski et al., 1996), and Vostok (MacGregor et al., 2009); See MacGregor et al. (2007, 2009) for

more details on the temperature and chemical datasets for Siple Dome and Vostok, respectively, as well as methods to derive radar-effective values at all of these sites. Depth-averaged radar-effective acidities (salinities) at these sites are $1.2 \mu\text{M}$ ($4.1 \mu\text{M}$) at Siple Dome, $1.7 \mu\text{M}$ ($0.6 \mu\text{M}$) at the South Pole, $1.6 \mu\text{M}$ ($0.7 \mu\text{M}$) at Taylor Dome, and $0.5 \mu\text{M}$ ($2.0 \mu\text{M}$) at Vostok.

Ionic concentrations in the near-surface snow depend on surface elevation, distance from the coast, surface accumulation rate, and surface temperature (Bertler et al., 2005). We also found that the depth-averaged acidity and salinity at the ice-core sites depend on these parameters. Acidity correlates the strongest to the surface accumulation rate (regression coefficient $r=0.41$), whereas salinity correlates the strongest to surface elevation ($r=0.55$). We used these correlations to approximate the depth-averaged acidity and salinity across the Antarctic ice sheet. The resulting acidity ranges between 0 and $35 \mu\text{M}$ (contours for $1\text{--}3 \mu\text{M}$ in Fig. 9b), whereas the salinity ranges between 0.1 and $4.2 \mu\text{M}$. In terms of attenuation rate, the salinity range is equivalent to acidities of only $0\text{--}0.6 \mu\text{M}$. Moreover, the higher salinities are predicted at low surface elevations, where higher ice temperatures typically reduce the sea salt contribution to attenuation compared to that from pure ice (Fig. 1a). Therefore, we ignore the contribution to attenuation from sea salts and focus on the contribution from acids. This approximation is more appropriate in the inland elevated area with thicker ice, which is our region of primary interest.

More sophisticated methods have been developed to estimate the effects of chemistry upon attenuation, such as that applied to a Vostok flowline (MacGregor et al., 2012). Such methods require spatial patterns of (modeled or radar-observed) englacial isochrones and knowledge of the surface chemistry over space and time. However, englacial isochrones have not yet been mapped across the entire Antarctic ice sheet and relatively few ice cores exist. We therefore consider results from our present attenuation model to be a first-order prediction for the whole of the ice sheet.

3.4.3. Spatial pattern of the acid contribution

First, we assume that acidity is uniformly $1 \mu\text{M}$ and calculate the fractional contribution from $\langle N_{\text{acid}} \rangle$ to that of pure-ice $\langle N_{\text{pure}} \rangle$ for the ensemble-mean temperature field. Because acidity and pure-ice components have similar magnitudes at low temperatures (Fig. 1a), acids have a relatively high contribution in areas where the ice sheet is relatively cold and thin (Fig. 9a). In inland East Antarctica, shallow ice is cold (Fig. 2a) but the thickness of warmer, deep ice is significant, making the contribution from acidity relatively small.

Next, we calculated the $\langle N_{\text{acid}} \rangle / \langle N_{\text{pure}} \rangle$ ratio for the spatially variable acidity contribution estimated from ice cores and the ensemble-mean temperature field. In coastal areas, where acidity often exceeds $2\text{--}3 \mu\text{M}$, the contribution from acid is predicted to be comparable to that from pure ice (Fig. 9b). For inland regions, the acidity contribution varies between 10% and 30% of the pure-ice contribution in East Antarctica, and 30% and 70% in West Antarctica. Comparison of Fig. 9a and b shows that both ice temperature and acidity distribution similarly affect the continent-wide distribution of the $\langle N_{\text{acid}} \rangle / \langle N_{\text{pure}} \rangle$ ratio. We also found that, in the upper half of the ice sheet where ice is relatively cold, $\langle N_{\text{acid}} \rangle_0^{0.52H}$ is often as large as $\langle N_{\text{pure}} \rangle_0^{0.52H}$ (not shown in figures), but the magnitude is much smaller than that at greater depths. On average, 16%–68% of acid-origin attenuation occurs in the deeper half of the ice sheet, whereas the remaining 32%–84% is localized in the shallower half of the ice sheet. Therefore, regardless of the depth, knowledge of englacial chemistry for the entire ice column is important.

In the real ice sheet, the total attenuation equals the sum of the pure-ice and chemical contributions: $\langle N_{\text{total}} \rangle = \langle N_{\text{pure}} \rangle + \langle N_{\text{acid}} \rangle$

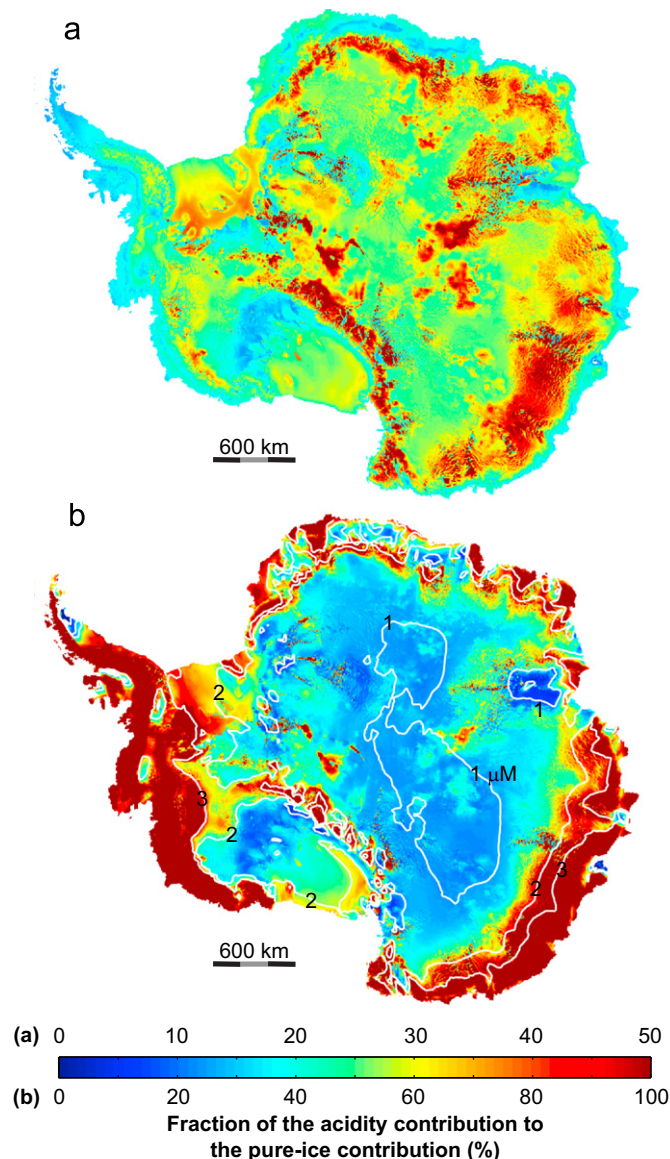


Fig. 9. Fraction of the acidity contribution to attenuation $\langle N_{\text{acid}} \rangle$ to the pure-ice contribution $\langle N_{\text{pure}} \rangle$, (a) for a depth-averaged acidity fixed at $1 \mu\text{M}$, and (b) based on the modeled depth-averaged acidity distribution using deep ice cores. Contours show acidities of 1, 2, and $3 \mu\text{M}$. Both estimates use the ensemble-mean temperature field, which was used to estimate the pure-ice contribution in Fig. 7. The color scale is different for (a) and (b).

(+ $\langle N_{\text{sea salt}} \rangle$). The chemical components contribute 26% of $\langle N_{\text{total}} \rangle$ at Siple Dome (MacGregor et al., 2007) and 21% of $\langle N_{\text{total}} \rangle$ at Vostok (MacGregor et al., 2009). Similarly, we estimated that, on average, $\langle N_{\text{acid}} \rangle = 0.29 \langle N_{\text{total}} \rangle$ in the inland area, where the acidity is less than 2 μM , and $\langle N_{\text{acid}} \rangle = 0.53 \langle N_{\text{total}} \rangle$ in the coastal area where the acidity exceeds 2 μM .

4. Discussion

The results presented here largely depend on the accuracy of the dielectric parameterization (Eq. (5), Fig. 1). Unfortunately, measurements are particularly sparse above -10°C and measured ice conductivities vary widely. A standard deviation between such measurements (table 1 in MacGregor et al., 2007) can result in attenuation difference equivalent to 2–4 μM variations in the acidity (Fig. 1a). Therefore, conductivity measurements are needed especially to thoroughly constrain the pure-ice contribution at temperatures above -10°C .

Our one-dimensional modeling illustrates the high sensitivity of the attenuation to the boundary conditions when the bed is barely frozen (Figs. 3–5). In the real ice sheet, horizontal advection of heat reduces the horizontal gradients in the temperature field and thus the attenuation field. The attenuation field has been found not to vary abruptly across the shore of a subglacial lake (MacGregor et al., 2012) or across a grounding zone (Matsuoka et al., 2012b). Nevertheless, the three-dimensional modeling presented here shows that a combination of the modest variability of $\langle N \rangle$ and thick ice in inland regions can easily compromise bed diagnoses from radar (Fig. 7). Therefore, one can potentially interpret an abrupt change in the bed-returned power over distances of several ice thicknesses as delineating a boundary between a thawed and a frozen bed. But caution is needed especially when the bed is barely frozen, which can occur in the vicinity of ice streams, subglacial lakes, and grounding zones.

Gradual changes in the bed reflectivity can occur, for instance, when the basal-melt rate is small and melt water gradually accumulates through a subglacial hydraulic network (Wright et al., 2012). Describing such networks is crucial for understanding how subglacial water affects ice-sheet dynamics. When the bed-returned power varies more gradually over a longer horizontal distance, it becomes much harder to distinguish between a change in bed reflectivity and a change in attenuation. Over horizontal distances of 50–400 km, the surface accumulation rate can easily vary between 0.1 and 0.2 m/a (Fig. 2c), which can change $\langle N \rangle$ by 2–8 dB/km (Fig. 4), thus changing L by 12–48 dB for 3-km-thick ice. Such accumulation-rate variations can be inferred from depth patterns of englacial reflectors that have been widely accepted as isochrones (e.g., Waddington et al., 2007). Combined analysis of the radar returned power and radar stratigraphy can thus help avoid incorrect diagnosis of the bed conditions. However, geothermal-flux patterns remain largely unknown. When the geothermal-flux variations are large enough to compromise the bed diagnosis, associated basal melting rates are too small to clearly modify the depth patterns of the isochrones (Matsuoka, 2011). Therefore, it is virtually impossible to detect attenuation variations caused by geothermal flux except for extreme cases that have produced down-warping radar reflectors through anomalously large basal melting (e.g., Fahnestock et al., 2001).

Two algorithms have been used to estimate englacial attenuation and then bed reflectivity using radar-profiling data. The more widely-used algorithm assumes that the geometrically corrected returned power $[P^c]_{\text{dB}}$ linearly depends on ice thickness (e.g., Jacobel et al., 2009). Half of the least-square-sense gradient,

$\langle [P^c]_{\text{dB}}/dH \rangle/2$, is then interpreted as the regional-mean attenuation rate. The other algorithm uses spatial variations in the returned power of both the single- and the double-bounced echoes (MacGregor et al., 2011). For both methods, the ice-thickness range should be large enough that the two-way attenuation L is significantly larger than both the noise and spatial variation in the bed reflectivity (Eq. (2)). For ice thicker than 2 km, $\langle N \rangle$ averages roughly 10 dB/km (Fig. 7), implying that the ice thickness must vary by at least several hundred meters to ensure a robust attenuation estimate. However, for an ice-thickness change of 0.5 km, L in 3-km-thick ice could easily vary by 3–4.5 dB when the bed is either completely frozen or thawed and ~ 9 dB when the bed is barely frozen (Fig. 6). Also, the bed is more likely to be thawed under thicker ice, so both the englacial attenuation and basal reflectivity are inherently related to the ice thickness, which further complicates robust estimation of attenuation using these methods.

Attenuation estimates based on the three-dimensional ice-temperature fields (Figs. 7–9) can be used to examine the first-order, continent-wide attenuation distributions. However, this method cannot be used alone to deduce the bed conditions from radar data, because the method that predict englacial attenuation good enough should adequately predict the basal conditions as well (so radar measurements are no longer necessary to constrain the bed conditions). In reality, the model predictions have significant uncertainties due to poor knowledge of both the boundary conditions and of the ice-sheet evolution. A recent observation in central West Antarctica shows that the depth-averaged attenuation rates in the top one third to half of the ice sheet vary by 5 dB/km over 120-km-long radar profiles across an ice-flow divide (Matsuoka et al., 2010). In that area, the surface accumulation rate has a large lateral gradient (Morse et al., 2002) and both ice-sheet evolution and ice chemistry probably add further uncertainty to the attenuation field.

Ultimately, understanding the subglacial environment in Antarctica will require a combination of methods. Common-midpoint radar surveys can be used to constrain ice temperature (Winebrenner et al., 2003). Seismic data have similar potential (Peters et al., 2012). Use of a rapid ice drilling system should provide opportunities to measure geothermal flux underneath the ice sheet and to potentially log depth profiles of low-resolution acidity using a wall-attached device, which are two of the primary contributors to uncertainty in attenuation predictions. Currently, radar stratigraphy and returned power are interpreted separately, but we have shown that there is a motivation to conduct these interpretations simultaneously. In practice, they can be made iteratively towards the best possible estimates of the glaciological conditions in space and time. In the future, we expect that formal inverse problems will be formulated to simultaneously interpret all aspects of the radar data as well as other geophysical and geochemical data.

5. Conclusions

The depth-averaged attenuation rate $\langle N \rangle$ is most sensitive to the surface accumulation rate and geothermal flux when the ice-sheet bed is barely frozen (i.e. basal temperature is close to the pressure melting point). Specifically, $\langle N \rangle$ varies by up to 1 dB/km for either a surface accumulation rate variation of 1 cm/a or a geothermal flux variation of 5 mW/m². These sensitivities are even higher when both the surface accumulation rate and geothermal flux are low. In contrast, when the bed is thawed, $\langle N \rangle$ becomes independent of geothermal flux and insensitive to the surface accumulation rate. As the ice thickens, $\langle N \rangle$ increases if the bed is frozen but decreases when the bed is thawed. These

trends can result in large local variations in $\langle N \rangle$, which can jeopardize the accuracy of estimates of regional-mean $\langle N \rangle$ from radar data.

Uncertainty in $\langle N \rangle$ over present-day Antarctica is dominated by uncertainty in the geothermal flux. In inland East Antarctica, $\langle N \rangle$ uncertainties can lead to more than 10-dB variations in the two-way attenuation to the bed, a value roughly equal to the expected range of bed reflectivity. These predictions are based on the pure-ice contribution only; the spatially variable acidity and salinity adds further uncertainty. Our estimates show that the acid contribution to attenuation equals $\sim 29\%$ (inland) and $\sim 53\%$ (coast) of the total attenuation, whereas the sea-salt contribution is negligible. The acid contributes nearly equally at all depths, so low-resolution ice chemistry data for the entire ice thickness is important for attenuation modeling.

All of these attenuation predictions depend critically on the accuracy of conductivity parameterization; uncertainty in this parameterization results in uncertainty in the attenuation. More studies of dielectric measurements are needed, especially at temperatures above -10°C , because warm ice contributes greater uncertainty to attenuation predictions than cold ice.

Acknowledgments

We thank E.D. Waddington and T.A. Neumann for providing the one-dimensional numerical temperature model. Comments from two anonymous reviewers improved the paper. This work is supported by the Center for Ice, Climate, Ecosystems at the Norwegian Polar Institute and forms part of the ARC–ULB project Icecube–Dyn at the Université Libre de Bruxelles.

References

- Bentley, C.R., Lord, N., Liu, C., 1998. Radar reflections reveal a wet bed beneath stagnant Ice Stream C and a frozen bed beneath ridge BC, West Antarctica. *J. Glaciol.* 44, 149–156.
- Bertler, N., Mayewski, P.A., Aristarain, A., et al., 2005. Snow chemistry across Antarctica. *Ann. Glaciol.* 41, 167–179.
- Carter, S.P., Blankenship, D.D., Peters, M.E., Young, D.A., Holt, J.W., Morse, D.L., 2007. Radar-based subglacial lake classification in Antarctica. *Geochem. Geophys.* 8, Q03016, <http://dx.doi.org/10.1029/2006gc001408>.
- Carter, S.P., Blankenship, D.D., Young, D.A., Holt, J.W., 2009. Using radar-sounding data to identify the distribution and sources of subglacial water: application to Dome C, East Antarctica. *J. Glaciol.* 55, 1025–1040.
- Cole Dai, J., 2004. Sulfate-Based Volcanic Record from South Pole Ice Cores. National Snow and Ice Data Center.
- Comiso, J.C., 2000. Variability and trends in Antarctic surface temperatures from in situ and satellite infrared measurements. *J. Clim.* 13, 1674–1696.
- Fahnestock, M., Abdalati, W., Joughin, I., Brozena, J., Gogineni, P., 2001. High geothermal heat row, basal melt, and the origin of rapid ice flow in central Greenland. *Science* 294, 2338–2342.
- Fox-Maule, C., Purucker, M.E., Olsen, N., Mosegaard, K., 2005. Heat flux anomalies in Antarctica revealed by satellite magnetic data. *Science* 309, 464–467.
- Fricke, H.A., Scambos, T., Bindschadler, R., Padman, L., 2007. An active subglacial water system in West Antarctica mapped from space. *Science* 315, 1544–1548.
- Fujita, S., Holmlund, P., Matsuoka, K., Enomoto, H., Fukui, K., Nakazawa, F., Sugiyama, S., Surdyk, S., 2012. Radar diagnosis of the subglacial conditions in Dronning Maud Land, East Antarctica. *The Cryosphere* 6, 1203–1219, <http://dx.doi.org/10.5194/tc-6-1203-2012>.
- Fujita, S., Maeno, H., Matsuoka, K., 2006. Radio-wave depolarization and scattering within ice sheets: a matrix-based model to link radar and ice-core measurements and its application. *J. Glaciol.* 52, 407–424.
- Fujita, S., Matsuoka, T., Ishida, T., Matsuoka, K., Mae, S., 2000. A summary of the complex dielectric permittivity of ice in the megahertz range and its applications for radar sounding of polar ice sheets. In: Hondoh, T. (Ed.), *Physics of Ice Core Records*. Hokkaido University Press, Sapporo, pp. 185–212.
- Gray, L., Joughin, I., Tulaczyk, S., Spikes, V.B., Bindschadler, R., Jezek, K., 2005. Evidence for subglacial water transport in the West Antarctic Ice Sheet through three-dimensional satellite radar interferometry. *Geophys. Res. Lett.* 32, L03501.
- Gudmandsen, P., 1971. Electromagnetic probing of ice. In: Wait, J. (Ed.), *Electromagnetic Probing in Geophysics*. Golem Press, Boulder, CO, pp. 321–348.
- Huybrechts, P., 2002. Sea-level changes at the LGM from ice-dynamic reconstructions of the Greenland and Antarctic ice sheets during the glacial cycles. *Quat. Sci. Rev.* 21, 203–231.
- Jacobel, R., Welch, B.C., Osterhouse, D., Pettersson, R., MacGregor, J.A., 2009. Spatial variation of radar-derived basal conditions on Kamb Ice Stream. *West Antarctica Ann. Glaciol.* 50, 10–16.
- Jacobel, R.W., Lapo, K.E., Stamp, J.R., Youngblood, B.W., Welch, B.C., Bamber, J.L., 2010. A comparison of basal reflectivity and ice velocity in East Antarctica. *Cryosphere* 4, 447–452.
- Le Brocq, A.M., Payne, A.J., Vieli, A., 2010. An improved Antarctic dataset for high resolution numerical ice sheet models (ALBMAP v1). *Earth Syst. Sci. Data* 2, 247–260.
- MacGregor, J.A., Matsuoka, K., Waddington, E.D., Winebrenner, D.P., Pattyn, F., 2012. Spatial variation of englacial radar attenuation: modeling approach and application to the Vostok flowline. *J. Geophys. Res.* 117, F03022, <http://dx.doi.org/10.1029/2011JF002327>.
- MacGregor, J.A., Anandakrishnan, S., Catania, G., Winebrenner, D.P., 2011. The grounding zone of the Ross Ice Shelf, West Antarctica, from ice-penetrating radar. *J. Glaciol.* 57 (205), 917–928.
- MacGregor, J.A., Matsuoka, K., Studinger, M., 2009. Radar detection of accreted ice over Lake Vostok, Antarctica. *Earth Planet. Sci. Lett.* 282, 222–233.
- MacGregor, J.A., Winebrenner, D.P., Conway, H., Matsuoka, K., Mayewski, P.A., Clow, G.D., 2007. Modeling englacial radar attenuation at Siple Dome, West Antarctica, using ice chemistry and temperature data. *J. Geophys. Res.—Earth Surf.* 112, F03008, <http://dx.doi.org/10.1029/2006JF000717>.
- Matsuoka, K., Power, D., Fujita, S., Raymond, C.F., 2012a. Rapid development of anisotropic ice-crystal-alignment fabrics inferred from englacial radar polarimetry, central West Antarctica. *J. Geophys. Res.* 117 (F3), F03029, <http://dx.doi.org/10.1029/2012JF002440>.
- Matsuoka, K., Pattyn, F., Callens, D., Conway, H., 2012b. Radar characterization of the basal interface across the grounding zone of an ice-rise promontory in East Antarctica. *Ann. Glaciol.* 53, 29–36.
- Matsuoka, K., 2011. Pitfalls in radar diagnosis of ice-sheet bed conditions: lessons from englacial attenuation models. *Geophys. Res. Lett.* 38, L05505, <http://dx.doi.org/10.1029/2010GL046205>.
- Matsuoka, K., Morse, D., Raymond, C.A., 2010. Estimating englacial radar attenuation using depth profiles of the returned power, central West Antarctica. *J. Geophys. Res.—Earth Surf.* 115, F0212.
- Mayewski, P.A., Twickler, M.S., Whitlow, S.I., Meeker, L.D., Yang, Q., Thomas, J., Kreutz, K., Grootes, P.M., Morse, D.L., Steig, E.J., Waddington, E.D., Saltzman, E.S., Whung, P.-Y., Taylor, K.C., 1996. Climate change during the last deglaciation in Antarctica. *Science* 272, 1636–1638.
- Monaghan, A.J., Bromwich, D.H., Fogt, R.L., Wang, S.H., Mayewski, P.A., Dixon, D.A., Ekaykin, A., Frezzotti, M., Goodwin, I., Isaksson, E., Kaspari, S.D., Morgan, V.I., Oerter, H., Van Ommen, T.D., Van der Veen, C.J., Wen, J.H., 2006. Insignificant change in Antarctic snowfall since the International Geophysical Year. *Science* 313, 827–831.
- Moore, J.C., Fujita, S., 1993. Dielectric-properties of ice containing acid and salt impurity at microwave and low-frequencies. *J. Geophys. Res.—Solid Earth* 98, 9769–9780.
- Morse, D.L., Blankenship, D.D., Waddington, E.D., Neumann, T.A., 2002. A site for deep ice coring in West Antarctica: results from aerogeophysical surveys and thermo-kinematic modeling. *Ann. Glaciol.* 35, 36–44.
- Neumann, T.A., Conway, H., Price, P.B., Waddington, E.D., Catania, G., Morse, D.L., 2008. Holocene accumulation and ice-sheet dynamics in central West Antarctica. *J. Geophys. Res.* 113, F02018, <http://dx.doi.org/10.1029/2007JF000764>.
- Pattyn, F., 2003. A new three-dimensional higher-order thermomechanical ice sheet model: basic sensitivity, ice stream development, and ice flow across subglacial lakes. *J. Geophys. Res.—Solid Earth* 108, 2382.
- Pattyn, F., 2010. Antarctic subglacial conditions inferred from a hybrid ice sheet/ice stream model. *Earth Planet. Sci. Lett.* 295, 451–461.
- Peters, L.E., Anandakrishnan, S., Alley, R.B., Voigt, D.E., 2012. Seismic attenuation in glacial ice: a proxy for englacial temperature. *J. Geophys. Res.* 117, F02008.
- Peters, M.E., Blankenship, D.D., Morse, D.L., 2005. Analysis techniques for coherent airborne radar sounding: application to West Antarctic ice streams. *J. Geophys. Res.—Solid Earth* 110, B06303, <http://dx.doi.org/10.1029/2004JB003222>.
- Pollard, D., DeConto, R.M., Nyblade, A.A., 2005. Sensitivity of Cenozoic Antarctic ice sheet variations to geothermal heat flux. *Global Planet. Change* 49, 63–74.
- Payne, A.J., Huybrechts, P., Abe-Ouchi, A., Calov, R., Fastook, J.L., Greve, R., Marshall, S.J., Marsiati, I., Ritz, C., Tarasov, L., Thomassen, M.P.A., 2000. Results from the EISMINT model intercomparison: the effects of thermomechanical coupling. *J. Glaciol.* 46, 227–238.
- Rignot, E., Mouginot, J., Scheuchl, B., 2011. Ice flow of the Antarctic ice sheet. *Science* 333, 1427–1430.
- Rippin, D.M., Bamber, J.L., Siegert, M.J., Vaughan, D.G., Corr, H.F.J., 2004. The role of ice thickness and bed properties on the dynamics of the enhanced-flow tributaries of Bailey Ice Stream and Slessor Glacier, East Antarctica. *Ann. Glaciol.* 39, 366–372.
- Shapiro, N.M., Ritzwoller, M.H., 2004. Inferring surface heat flux distributions guided by a global seismic model: particular application to Antarctica. *Earth Planet. Sci. Lett.* 223, 213–224.
- Siegert, M.J., Carter, S., Tabacco, I., Popov, S., Blankenship, D.D., 2005. A revised inventory of Antarctic subglacial lakes. *Antarct. Sci.* 17, 453–460.
- Smith, B.E., Fricker, H.A., Joughin, I.R., Tulaczyk, S., 2009. An inventory of active subglacial lakes in Antarctica detected by ICESat (2003–2008). *J. Glaciol.* 55, 573–595.
- Stearns, L.A., Smith, B.E., Hamilton, G.S., 2008. Increased flow speed on a large East Antarctic outlet glacier caused by subglacial floods. *Nat. Geosci.* 1, 827–831.
- Van de Berg, W.J., van den Broeke, M.R., Reijmer, C.H., van Meijgaard, E., 2006. Reassessment of the Antarctic surface mass balance using calibrated output of a regional atmospheric climate model. *J. Geophys. Res.—Atmos.* 111, D11104.

- Waddington, E.D., Neumann, T.A., Koutnik, M.R., Marshall, H.P., Morse, D.L., 2007. Inference of accumulation-rate patterns from deep layers in glaciers and ice sheets. *J. Glaciol.* 53, 694–712.
- Walker, R.T., Holland, D.M., 2007. A two-dimensional coupled model for ice shelf-ocean interaction. *Ocean Model.* 17, 123–139.
- Winebrenner, D.P., Smith, B.E., Catania, G.A., Conway, H.B., Raymond, C.F., 2003. Radio-frequency attenuation beneath Siple Dome, West Antarctica, from wide-angle and profiling radar observations. *Ann. Glaciol.* 37, 226–232.
- Wingham, D.J., Siegert, M.J., Shepherd, A., Muir, A.S., 2006. Rapid discharge connects Antarctic subglacial lakes. *Nature* 440, 1033–1036.
- Wright, A.P., Young, D.A., Roberts, J.L., Schroeder, D.M., Bamber, J.L., Dowdeswell, J.A., Young, N.W., Le Brocq, A.M., Warner, R.C., Payne, A.J., Blankenship, D.D., van Ommen, T.D., Siegert, M.J., 2012. Evidence of a hydrological connection between the ice divide and ice sheet margin in the Aurora Subglacial Basin, East Antarctica. *J. Geophys. Res.—Earth Surf.* 117, 15.